Atmos. Meas. Tech. Discuss., 8, 10429–10471, 2015
www.atmos-meas-tech-discuss.net/8/10429/2015/
doi:10.5194/amtd-8-10429-2015

Atmospheric Measurement Techniques Discussions

Lidar arc scan uncertainty reduction through scanning geometry optimization

H. Wang[1], R. J. Barthelmie[1], S. C. Pryor[2], and G. Brown[3]

[1]Sibley School of Mechanical and Aerospace Engineering, Cornell University, Ithaca, New York, USA
[2]Department of Earth and Atmospheric Sciences, Cornell University, Ithaca, New York, USA
[3]SgurrEnergy Ltd, Vancouver, British Columbia, Canada

Received: 24 June 2015 – Accepted: 3 September 2015 – Published: 7 October 2015

Correspondence to: H. Wang (hw524@cornell.edu)

Published by Copernicus Publications on behalf of the European Geosciences Union.

Abstract

Doppler lidars are frequently operated in a mode referred to as arc scans, wherein the lidar beam scans across a sector with a fixed elevation angle and the resulting measurements are used to derive an estimate of the *n* minute horizontal mean wind velocity (speed and direction). Previous studies have shown that the uncertainty in the measured wind speed originates from turbulent wind fluctuations and depends on the scan geometry (the arc span and the arc orientation). This paper is designed to provide guidance on optimal scan geometries for two key applications in the wind energy industry: wind turbine power performance analysis and annual energy production. We present a quantitative analysis of the retrieved wind speed uncertainty derived using a theoretical model with the assumption of isotropic and frozen turbulence, and observations from three sites that are onshore with flat terrain, onshore with complex terrain and offshore, respectively. The results from both the theoretical model and observations show that the uncertainty is scaled with the turbulence intensity such that the relative standard error on the 10 min mean wind speed is about 30 % of the turbulence intensity. The uncertainty in both retrieved wind speeds and derived wind energy production estimates can be reduced by aligning lidar beams with the dominant wind direction, increasing the arc span and lowering the number of beams per arc scan. Large arc spans should be used at sites with high turbulence intensity and/or large wind direction variation when arc scans are used for wind resource assessment.

1 Introduction

Coherent Doppler lidars (CDL, hereafter called lidars) have been used to probe a range of atmospheric boundary layer (ABL) phenomena, including nocturnal low level jets in the Great Plains (Banta et al., 2008), spatial variability of wind in the marine ABL (Pichugina et al., 2012), structures of the urban ABL (Calhoun et al., 2006; Frehlich et al., 2006) and turbulent properties and flow patterns over complex terrain (Krish-

AMTD
8, 10429–10471, 2015

namurthy et al., 2011; Choukulkar et al., 2012). Lidars also have applications in wind energy resource estimation and wake characterization (Banta et al., 2013; Barthelmie et al., 2013) due to their ability to accurately and precisely measure flow structures both in front of and in the wake of a wind turbine (Simley et al., 2013; Aitken et al., 2014) and spatial variability of wind speeds over prospective wind farms (Krishnamurthy et al., 2013).

Lidar measurements usually involve operating the instrument with a scan geometry to acquire radial velocities from at least three locations and estimating the wind velocity according to the following equation:

$$v_r(r) = \boldsymbol{d}^T \boldsymbol{u} \quad (1)$$

where $\boldsymbol{d}^T = [\cos\phi\sin\theta, \cos\phi\cos\theta, \sin\phi]$ and $\boldsymbol{u}^T = [u, v, w,]$. The radial velocity v_r is the projection of the wind velocity $\boldsymbol{u}$ on the line of sight (LOS) at the position $r = r\boldsymbol{d}$ for which r is the range distance from the lidar along the LOS and $\boldsymbol{d}$ is the unit directional vector determined by the elevation angle ϕ and the azimuth angle θ of the LOS from north. The uncertainty in the estimated wind velocity has great importance to wind energy applications and is a function of the atmospheric turbulence structure and the specific lidar scanning geometry (Banakh et al., 1995). Two common scanning geometries applied in wind energy are the Velocity-Azimuth-Display (VAD) scan and the arc scan. VAD scans apply a full-azimuth conical scan (i.e. θ from 0 to 360°) with a constant elevation angle (ϕ) and the wind velocity is estimated using least squares to solve Eq. (1) under the assumption of a horizontally homogeneous wind field. When these assumptions are met VAD scans are reliable and well understood and can meet the stringent accuracy requirement for wind energy applications (Gottschall et al., 2012). The arc scan involves ϕ being held constant and θ varied to sample a conical sector (e.g. Henke and Clive, 2015). VAD scans are commonly used for wind resource assessment because in homogeneous terrain or under a constant wind gradient the function used to derive the wind velocity should have the smallest errors while arc scans can potentially have large errors if the fit is distorted by a small number of erroneous points.

AMTD
8, 10429–10471, 2015

However, arc scans "are less affected by inhomogeneities in the wind field on scales of the scan diameter than are the full circle scans" (Schwiesow et al., 1985). Arc scans have a role, especially if heterogeneous conditions exist, because of the scan can be focused on the region of interest. For example, a conical scan centered at the hub of an operating wind turbine will be affected by inhomogeneity because of the wind turbine wake and the scale of inhomogeneity (the size of wake) is smaller than the diameter of the conical scan. If the purpose of measurement is the freestream wind speed, a smaller sector scan or arc scan upwind of the wind turbine can be more accurate than a full conical scan. Arc scans also has the advantage that by only sampling the area of interest the number of sample repetitions in a given time can be increased, decreasing the statistical uncertainty in solving Eq. (1). Use of arc scans adds two additional parameters to the scanning geometry: (1) the arc span (i.e. the width of the scan sector, $\Delta\theta$) and (2) the angle between the center of the arc and the wind direction which is a measure of the orientation of the arc scan and will be called hereafter the relative direction and denoted as β. The selection of these parameters have implications for the accuracy of the retrieved wind speed (Courtney et al., 2014; Wang et al., 2015). Here we extend prior work on optimizing scan geometry to minimize the uncertainty in the estimated wind speeds. We present a quantitative analysis of the dependence of the retrieved wind speed uncertainty on the scanning geometry and the turbulence intensity, and provide a tool for use in planning lidar deployments for wind energy applications such as power performance tests. The analysis uses both a theoretical turbulence model and real arc scan measurements from a pulsed lidar deployed in three different geographic locations characterized by different surface roughness and turbulence regimes. We conclude by demonstrating how the wind speed uncertainty from arc scans propagates through into uncertainty in predictions of the annual energy production (AEP).

AMTD
8, 10429–10471, 2015

2 Uncertainty in the lidar radial velocity

Uncertainties in measured radial velocities from a pulsed lidar (e.g. Sgurr's Galion lidar from which measurements are presented herein, Table 1) are well characterized (Frehlich and Yadlowsky, 1994; Frehlich, 1997) and can be described as follows:

$$v_R = \langle v_R \rangle + e + \delta \quad (2)$$

where v_R is the measured radial velocity, $\langle v_R \rangle$ is the true radial velocity in the sensing volume, δ is the bias due to systematic errors and e is the random error which has zero mean and variance σ_e^2. The magnitude of σ_e^2 is a function of both the signal-to-noise ratio (SNR) and the radial velocity variance ($\sigma_{v_r}^2$) in the sensing volume. The true radial velocity in a sensing volume centered at a range distance r is well approximated by the weighted average of the radial velocities in the sensing volume as

$$\langle v_R(r) \rangle = \int_0^\infty v_r(s) W(r-s) \mathrm{d}s \quad (3)$$

where s is the distance from the lidar along the LOS, and $W(r-s)$ is a weighting function with its peak value at $s = r$. Note that we use v_r to denote a radial velocity at a point location and v_R a measured (volumetrically averaged) radial velocity.

The precision of v_R is bounded by the Cramer–Rao Bound (CRB) which is a function of SNR (Pearson and Collier, 1999). The relationship between CRB and SNR derived from Eq. (5) in Pearson and Collier (1999), and that estimated from a time series of radial velocity measurements derived using the autocorrelation method from Frehlich (2001) are shown in Fig. 1 for the Galion lidar. Both show that CRB decreases exponentially with increasing SNR, and for the Galion lidar, σ_e^2 has the lower bound of $0.01\,\mathrm{m^2\,s^{-2}}$ when SNR > −20 dB.

The uncertainty in v_R also scales with the atmospheric turbulence intensity because turbulent fluctuations of both wind speed and locations of backscattering particles in

AMTD
8, 10429–10471, 2015

the sensing volume broaden the signal spectrum and thus increase the uncertainty in v_R (Banakh et al., 1995; Frehlich, 1997). When the turbulence is sufficiently strong, the random error variance σ_e^2 becomes insensitive to SNR, i.e., when $\sigma_{v_r} \geq 0.5 w_R$ (where w_R is the spectrum width of the lidar signal in velocity space, which for the Galion $\approx 0.877\,\mathrm{m\,s^{-1}}$), $\sigma_e^2 \propto \sigma_{v_r}^2$. If σ_{v_r} is extremely large, the spectrum width increases such that the peak is indistinguishable from the noise and the radial velocity selected by the estimator is a random value within the velocity search space ($\pm 39\,\mathrm{m\,s^{-1}}$ for the Galion lidar).

Other sources of errors in v_R include non-linear vertical wind shear which can introduce a bias in a radial velocity measurement (Lindelöw et al., 2008), and lidar misalignment which results in incorrect azimuth and elevation angles so the measured radial velocity does not represent the wind field at the intended location. For a well-secured ground-based lidar pitch (displacement from the horizontal) and roll (i.e. "tilt") angles rarely exceed 1°, causing negligible errors (e.g. Fig. 2), but pitch and roll are recorded for each measurement with the Galion lidar so that potential errors can be evaluated.

The synthesis given above thus indicates that when the SNR is reasonably high, and pitch and roll are close to zero, the uncertainty in v_R is $< 0.1\,\mathrm{m\,s^{-1}}$. Thus, these potential error sources make a much smaller contribution than the overall uncertainty in the derived horizontal wind speed than turbulent wind fluctuations in the sampling volume (as shown in the next section). Hence, the uncertainty in v_R will not be considered further in calculating the uncertainty in the estimated mean wind speed from arc scans.

3 Uncertainty in wind speeds derived from lidar arc scan measurements

As in other Eulerian measurement systems (e.g. a network of anemometers deployed on meteorological masts), a lidar conducting arc scans measures the wind velocity by sampling the wind field with a specified sampling frequency and spatial coverage, but the difference is that the lidar measures the radial velocity and the wind velocity needs to be estimated using an inverse method applied under certain assumptions about the

AMTD
8, 10429–10471, 2015

wind field. When the radial velocity has negligible errors, the uncertainty in the estimated wind velocity is controlled by (1) the spatial statistics of the wind field that determine the variation of, and the correlation between, the samples (and hence effective sample size, and the representativeness of the wind field), (2) the scanning geometry that determines the temporal and spatial resolution of the samples and (3) the stability of the inverse method. In this section, we describe how the uncertainty in the estimated mean horizontal wind speed from arc scans (denoted as $\hat{\boldsymbol{V}}_0$) is related to the characteristics of the wind field and the scanning geometry. The method used follows that of Banakh et al. (1995) which was used to evaluate the uncertainty of wind velocities estimated from VAD scans.

In a homogenous and stationary wind field, the covariance between the ith and jth radial velocities, which are measured by a lidar from the sensing volumes centered at r_i and r_j, respectively, is a function of the relative location between these two measurements. With the assumption of frozen turbulence, the relative position between the two measurements is $\boldsymbol{p}_{ij} = \boldsymbol{r}_i - \boldsymbol{r}_j - \Delta\boldsymbol{p}_{ij}$ where $\Delta\boldsymbol{p}_{ij} = [(i-j)\delta t]\boldsymbol{u}_0$ is the separation distance induced by the mean wind velocity $\boldsymbol{u}_0 = (u_0, v_0, w_0)$ during a time interval $(i-j)\delta t$. The covariance between the two measurements (a_{ij}) then can be written as

$$a_{ij}(\boldsymbol{p}_{ij}) = \iint_0^\infty [W(s_i - r_i)W(s_j - r_j)K_\mathrm{r}(\boldsymbol{q}_{ij})]\mathrm{d}s_i\mathrm{d}s_j \tag{4}$$

where $s_i = \boldsymbol{s}_i\boldsymbol{d}_i$, $s_j = \boldsymbol{s}_j\boldsymbol{d}_j$, and $\boldsymbol{q}_{ij} = \boldsymbol{s}_i - \boldsymbol{s}_j - \Delta\boldsymbol{p}_{ij}$. The term $K_\mathrm{r}(\boldsymbol{q}_{ij})$ is the covariance between the point radial velocities (v_r) separated by $\boldsymbol{q}_{ij}$ and it is related to the covariance matrix $\mathbf{C}(\boldsymbol{q}_{ij})$ of the wind velocity with the same separation distance:

$$K_\mathrm{r}(\boldsymbol{q}_{ij}) = \boldsymbol{d}_i^T\mathbf{C}(\boldsymbol{q}_{ij})\boldsymbol{d}_j \tag{5}$$

The entries in the covariance matrix **C** are the ensemble variance and covariance between three orthogonal wind components. Note no summation is assumed over repeated indices in Eqs. (4) and (5). Let **A** denote the covariance matrix for all the measured radial velocities within a 10 min period. The entry of **A** at ith row and jth column

AMTD
8, 10429–10471, 2015

is defined by Eq. (4). For a given scanning geometry, Eqs. (4) and (5) show that, apart from the atmospheric turbulence structure, the statistics of the measured radial velocities are controlled by the mean wind field because the separation distance $\Delta \boldsymbol{p}_{ij}$ or $\Delta \boldsymbol{q}_{ij}$ varies with the mean wind speed and direction (as illustrated in Fig. 3). When the relative angle β of the lidar beam relative to the flow = 0°/180° (westerly/easterly in Fig. 3), the samples are located in a rectangular area swept by the wind over the arc. When $\beta = \pm 90^{\circ}$ the samples are from a line aligned with the arc. If the scan direction is the same as the wind (i.e. $\beta = +90^{\circ}$), the samples from one arc scan are clustered and almost from the same location (northerly in Fig. 3). When $\beta = -90^{\circ}$, the locations sampled by one arc are more spatially extended (southerly in Fig 3.).

The uncertainty in the wind speed estimated for arc scans can be derived from the covariance matrix $\mathbf{A}$ of the measured radial velocities. Assuming a horizontally homogenous wind field with zero mean vertical wind speed (i.e. $w_0 = 0$), the horizontal wind velocity ($\boldsymbol{V}_0$) is estimated by solving the following equation with the least squares method

$$\mathbf{D}\boldsymbol{V}_0 = \boldsymbol{v}_{\mathrm{R}} \tag{6}$$

where $\boldsymbol{v}_{\mathrm{R}}$ is a vector including N radial velocities measured in, for example, 10 min and $\mathbf{D}$ is a $N \times 2$ matrix with its ith row given by $[\cos\phi \sin\theta_i, \cos\phi \cos\theta_i]$. The least squares solution is

$$\hat{\boldsymbol{V}}_0 = \mathbf{G}\boldsymbol{v}_{\mathrm{R}} \tag{7}$$

where

$$\mathbf{G} = (\mathbf{D}^{\mathrm{T}}\mathbf{D})^{-1}\mathbf{D}^{\mathrm{T}} \tag{8}$$

The estimated wind velocity $\hat{\boldsymbol{V}}_0$ comprises horizontal components, $\hat{\boldsymbol{V}}_0 = (\hat{u}_0, \hat{v}_0)$. The uncertainty in $\hat{\boldsymbol{V}}_0$ is characterized by its covariance matrix ($\hat{\mathbf{C}}$) given by

$$\hat{\mathbf{C}} = \mathbf{G}\mathbf{A}\mathbf{G}^{\mathrm{T}} \tag{9}$$

AMTD
8, 10429–10471, 2015

For most applications, the desired output from arc scans are the horizontal wind speed and direction. The horizontal wind speed ($\hat{V}_0$) is estimated from:

$$V_0 = \sqrt{\hat{u}_0^2 + \hat{v}_0^2} \tag{10}$$

The uncertainty in $\hat{V}_0$ as quantified by the standard error $\sigma_{\hat{V}}$ can be approximated as (Lyons, 1991)

$$\sigma_{\hat{V}} = \left[\left(\hat{u}_0\sigma_{\hat{u}_0}\right)^2 + \left(\hat{v}_0\sigma_{\hat{v}_0}\right)^2 + 2\left(\rho_{uv}\sigma_{\hat{u}_0}\sigma_{\hat{v}_0}\right)\left(\hat{u}_0\hat{v}_0\right)\right]^{0.5} / \hat{V}_0 \tag{11}$$

where $\sigma^2_{\hat{u}_0}$ and $\sigma^2_{\hat{v}_0}$ represent the variance of $\hat{u}_0$ and $\hat{v}_0$ and can be found from the diagonal of $\hat{\mathbf{C}}$, respectively. The term ρ_{uv} in Eq. (11) is the correlation between $\hat{u}_0$ and $\hat{v}_0$, and $\rho_{uv}\sigma_{\hat{u}_0}\sigma_{\hat{v}_0}$ is the covariance that is given by the only non-diagonal term in $\hat{\mathbf{C}}$. Note that the complete expression for the covariance matrix of $\hat{\boldsymbol{V}}_0$ should include the radial velocity measurement error:

$$\hat{\mathbf{C}} = \mathbf{G}\left(\mathbf{A} + \sigma_e^2\mathbf{I}\right)\mathbf{G}^{\mathrm{T}} \tag{12}$$

where $\mathbf{I}$ is the identity matrix. Because $\sigma_e^2 \sim 0.01\,\mathrm{m^2\,s^{-2}}$ (see Sect. 2), it is much smaller that the diagonal terms of $\mathbf{A}$ ($> 0.1\,\mathrm{m^2\,s^{-2}}$), and therefore is neglected in the following analysis.

4 Uncertainty computed from an isotropic turbulence model

Following the background presented in Sect. 3, below the uncertainty in a 10 min mean wind speed estimated from lidar arc scans is analyzed as a function of (1) turbulence intensity, (2) mean wind speed and direction, and (3) scanning geometry using an

AMTD
8, 10429–10471, 2015

isotropic turbulence model. For isotropic turbulence the covariance of the measured radial velocities in Eq. (4) can be calculated as follows: the entry at the lth row and kth column (l, k = 1, 2, 3) of the covariance matrix $\mathbf{C}(\boldsymbol{q})$ in Eq. (5) is given by the following equation (Monin and Yaglom (1965) cited in Banakh et al. (1995))

$$c_{lk}(\boldsymbol{q}) = c_u(q)\delta_{lk} + \frac{1}{2}q\frac{\mathrm{d}c_u}{\mathrm{d}q}\left(\delta_{lk} - \frac{q_l q_k}{q^2}\right) \tag{13}$$

where $q = |\boldsymbol{q}|$, q_1, q_2 and q_3 are the separation distances in the streamwise, transverse and vertical directions, respectively, and δ_{lk} is the Kronecker delta. The streamwise wind component spatial covariance function $c_u(q)$ can be approximated by the exponential decay function

$$c_u(q) = \sigma_u^2 \exp\left(-\frac{q}{L_u}\right) \tag{14}$$

where σ_u^2 is the streamwise velocity variance, and L_u is the turbulence integral length scale which can be calculated from turbulence intensity ($\mathrm{TI} = \sigma_u/V_0$) in a neutrally stratified atmospheric boundary layer (see Appendix A). Note Eq. (14) is inconsistent with the von Kármán model used to calculate L_u in Appendix A, but it has similar accuracy to the von Kármán model in predicting the uncertainty of wind speed from conical scans (Banakh et al., 1995). Thus, Eq. (14) is used here for its simplicity and effectiveness. For a given wind speed and direction, the separation distance vector $\boldsymbol{q}$ can be calculated from ϕ, $\delta\theta$ and r, and the point radial velocity covariance defined in Eq. (5) can be derived from Eqs. (13) and (14). Then the covariance of the measured radial velocities can be calculated by defining a weighting function in Eq. (4). In this analysis the weighting function is approximated by a triangular weighting function defined as

$$W(s-r) = \max\left[0, \frac{2}{\Delta R}\left(1 - \frac{2}{\Delta R}|s-r|\right)\right] \tag{15}$$

AMTD
8, 10429–10471, 2015

where ΔR is the spatial extent of v_R along the LOS, which is a function of the lidar pulse length and hence the illuminated volume at the time of measurement. For the Galion $\Delta R = 60$ m according to Frehlich (1997) and the lidar parameters in Table 1. The radial velocity covariance matrix **A** in Eq. (9) is calculated for N measured radial velocities and used in Eq. (11) for calculation of the associated uncertainty in $\hat{V}_0$ which is presented here as the relative standard error (abbreviated as RSE and denoted by ε) and is defined as the ratio of the standard error in the estimated mean horizontal wind speed to the true mean horizontal wind speed (V_0):

$$\varepsilon = \frac{\sigma_{\hat{V}}}{V_0} \tag{16}$$

which is a function of TI, and the mean wind speed and direction.

The relative importance of these functional dependencies and relevance to wind energy applications can be demonstrated using an example in which a lidar is used for a power performance test of a turbine. This type of test is undertaken to determine if the turbine is operating according to the specified power curve (i.e. production of electricity as a function of the inflow wind speed) and thus it involves measurements of the incident flow into the turbine rotor (Wagner et al., 2011). When lidars are used for this purpose they are typically deployed to measure with arc scans at the hub height three rotor diameters in front of the wind turbine. Assuming a hub height of 90 m and a rotor diameter of 90 m the lidar placed at the base of the turbine would be operated with a fixed elevation angle $\phi = 16.7^\circ$ and the area of interest is at the range distance $r = 313$ m. The arc scan is defined using a span of $\Delta\theta$ comprising M_θ azimuth angles. It takes δt seconds to finish one measurement at one azimuth angle and moves $\delta\theta$ to the next azimuth angle, so the sampling intervals are δt in time and $\delta\theta$ in space. As a result, one arc scan takes $M_\theta \delta t$ seconds and the total number of arc scans conducted in 10 min is $M_{10} = 600/M_\theta \delta t$. For the power performance test scenario described above typical parameters would be: $\delta t = 3$ s, $\Delta\theta = 30^\circ$ and $\delta\theta = 6^\circ$. For reasonable values of TI and V_0, using the isotropic turbulence model and the definition of the dominant length

AMTD
8, 10429–10471, 2015

scale L_u in Appendix A, the RSE (ε) shows the strongest dependence on TI (Fig. 4a), and increases from about 1.5 % for $V_0 = 7–9\,\mathrm{m\,s^{-1}}$ at TI = 5 % (a low turbulence environment such as might be experienced offshore) to 6–9 % for TI > 20 % (i.e. a high turbulence environment). The RSE (ε) for TI = 12 %, for a range of wind speeds (V_0) and relative direction (β) of −180 to 180° (Fig. 4b) indicates that under the assumption of isotropic turbulence ε varies with β but the variation is no more than ±2 % for the range of conditions shown in Fig. 4b. The relationships shown in Fig. 4b are expected because the sample locations and resulting spatial correlations between the samples are determined by the wind speed and direction (see Fig. 3). The RSE reaches its minimum at $\beta = 0$ and 180° and exhibits the lowest dependence on wind speed, because these relative directions result in a similar spatial distribution of the samples. The maximum ε occurs at $\beta = \pm 45$ and ±135° and exhibits a much stronger dependence on wind speed. When $\beta = \pm 90°$, ε reaches local minima and is has a relatively large difference because of the different spatial distribution and thus spatial correlation of samples between $\beta = -90$ and $\beta = +90°$ (see Fig. 3). The effect of scanning geometry on ε is such that ε decreases with increasing arc span ($\Delta\theta$) and decreasing beam number (or azimuth angles) per arc scan (Fig. 5). Enlarging $\Delta\theta$ increases the spatial coverage, and lowering the number of beams per arc scan increases the separation distance between samples, both of which reduce the correlation between samples and consequently the uncertainty in estimating the horizontal mean wind speed. Additionally, when $\Delta\theta$ increases and the beam number decreases, the condition number of the matrix **G** in Eq. (7) decreases and, as a result, the uncertainty introduced by the inverse method (the least squares method) decreases (Wang et al., 2015). The effect of scanning geometry on ε naturally exhibits a dependence on the relative direction (β). When the wind direction is parallel to the beams ($\beta = 0°$), ε is weakly dependent on both the arc span and the beam number (Fig. 5a). For example, with a fixed beam number, ε decreases by only 0.4 % when increasing $\Delta\theta$ from 30 to 120°. When $\beta = \pm 45°$, ε is less sensitive to the beam number than the arc span (Fig. 5b). When $\beta = \pm 90°$, ε is more sensitive to the beam number than the arc span (Fig. 5c and d). Sensitivity is the

AMTD
8, 10429–10471, 2015

highest when $\beta = +90^{\circ}$ and $\Delta\theta < 60^{\circ}$. When $\beta = +90^{\circ}$, there is a band of local minima with $\varepsilon < 4\,\%$ starting at $\Delta\theta = 30^{\circ}$ and beam number 8. The beam numbers and the arc spans associated with those minima are such that the distance between two adjacent azimuth angles is equal to the distance that the wind travels when the lidar changes from one azimuth angle to the next one. In other words, under the frozen turbulence assumption the lidar samples the same location repetitively, causing the uncertainty to reduce. The uncertainty in the wind speeds derived from arc scans naturally cause uncertainty in determining the wind speed corresponding to a power output and consequently uncertainty in the measured power curve. If the power coefficient (C_p) of wind turbine is invariant with wind speed, the uncertainty in the measured power curve is 3ε (because wind power is proportional to the cube of wind speed). Hence, neglecting other sources of uncertainty and error in wind turbine power performance test, such as shear across the swept area (Wagner et al., 2011), the analyses presented above imply that if the lidar beam is well aligned with the incoming "free stream", the uncertainty in the measured power curve for this example turbine and wind speeds of 7–9 $\mathrm{m\,s^{-1}}$ is about ±4 % for a site with low turbulence intensity (TI = 5 %) and ±20 % for a high turbulence intensity environment (TI = 20 %). Though these values of uncertainty resulting from lidar arc scans are similar to the uncertainties in the power curve measured with cup anemometers with the same turbulence characteristics (Wyngaard, 2010), using lidar arc scans can eliminate the uncertainty of cup anemometer measurements caused by meteorological mast flow distortion, which has a typical value of ±1 % in wind speed and therefore ±3 % in wind power (IEC, 2005).

5 Observed arc scan uncertainty

The theoretical uncertainty from the isotropic turbulence model presented in the previous section is a useful tool for decomposing the uncertainty by source, and potentially to aid in planning lidar scan geometries prior to onsite deployment. It is used here to contextualize empirical analyses of the uncertainty on the mean wind velocity, turbu-

AMTD
8, 10429–10471, 2015

lence statistics and scanning geometry using observational data derived from arc scan at three sites. Site names are not revealed because of confidentiality, but the site characteristics are provided below and the scan geometries are summarized in Fig. 6. In all cases the analysis is based on the estimated 10 min horizontal mean wind speed ($\hat{V}_0$) from the Galion measurements as derived using the ordinary least squares method and the relative error of $\hat{V}_0$ is defined as relative to measurements (V_c) from cup anemometers installed on nearby meteorological masts (in compliance with the standard IEC, 2005):

$$e_r = \frac{\hat{V}_0 - V_c}{V_c} \tag{17}$$

Periods with $V_c < 4\,m\,s^{-1}$ or lidar SNR < -20 dB are excluded from the analysis. The observed RSE ($\hat{\varepsilon}$) is defined as the standard deviation of e_r binned by wind direction or turbulence intensity, and the 95 % confidence interval, CI_{95}, of $\hat{\varepsilon}$ is estimated by (Ahn and Fessler, 2003)

$$CI_{95} = \hat{\varepsilon} \pm 1.96\hat{\varepsilon}/\sqrt{2(n-1)} \tag{18}$$

where n is he number of samples in a bin. Note that this definition means that only the spread of errors is evaluated and any bias is not considered.

It should be noted that the relative error defined in Eq. (17) is the difference between wind speed measured by the lidar and the cup anemometer. Thus, the observed RSE should have contributions from both the lidar and cup anemometer uncertainty, that is, by assuming errors from the lidars and the cup anemometers are independent,

$$\hat{\varepsilon} = \left(\varepsilon^2 + \varepsilon_c^2\right)^{1/2} \tag{19}$$

where ε_c is the relative error of cup anemometer. The cup anemometer uncertainty will be included in the following analysis and the relative error of the cup anemometer is

AMTD
8, 10429–10471, 2015

given by the following equation:

$$\varepsilon_c = \left(\frac{k}{\sqrt{3}}\right) \cdot \left(\frac{0.05\,m\,s^{-1}}{V_c} + 0.005\right) \quad (20)$$

where k is the cup anemometer class number representing the maximum relative error of cup anemometer (IEC, 2005). The k values for cup anemometers used at the three sites are listed in Table 2.

5.1 Site A

Site A is a wind farm on a flat barren land, approximately 20 km from a coastline and at a latitude of 27° N. The Galion lidar was operating for 20 days with arc scans centered at $\theta = 150°$ with $\Delta\theta = 120°$, $\delta\theta = 30°$ and $\phi = 18.32°$ (Fig. 6a). Wind speeds estimated from arc scan measurements at range gate 6 and 8 are evaluated against the concurrent data from cup anemometers installed on booms aligned southwest (227°) at 60 m height and 80 m height on a meteorological mast east of the lidar, respectively (Fig. 6a). Because of flow distortions from the wind turbines and the meteorological mast, the uncertainty evaluation is conducted only in the wind direction sector 90–165° (based on the wind vane measurement at 77 m on the meteorological mast), resulting in 952 and 775 measurements of 10 min mean wind speeds at 80 and 60 m height, respectively, and 100 % recovery rate at both heights.

The observed RSE($\hat{\varepsilon}$) at Site A calculated for 10° bins of β with V_c between 4 and 16 m s^{-1} is approximately 3 % and exhibits little dependence on β (Fig. 7). It is slightly higher at 60 m than at 80 m as the result of the lower mean wind speed and higher variance of wind speeds at 60 m. The small uncertainty is expected given the comparatively large arc span applied, and the values agree well with predictions based on the isotropic turbulence model applied using the observed mean wind speed and variance in each directional bin (Fig. 7). The predicted RSE (i.e. ε from Eq. 16) slightly underestimates the observed RSE (i.e. $\hat{\varepsilon}$) in most directional bins, but the underestimation

AMTD
8, 10429–10471, 2015

is well compensated by adding the relative error of the cup anemometer. The consistency between the predicted and observed relative errors indicates that turbulent wind fluctuations are the main source of uncertainty and the assumptions made in applying the isotropic turbulence model are largely realized.

5.2 Site B

Site B is an offshore wind farm at 54.0° N at which the Galion lidar made arc scans over a three month period centered at $\theta = 323.25°$ with $\Delta\theta = 30°$, $\delta\theta = 6°$ and $\phi = 5.75°$. Wind speeds retrieved from range gate 25 are evaluated against concurrent cup anemometer measurements collected on a boom oriented at 135° at 90 m on the meteorological mast north-northwest of the lidar (Fig. 6b). Observations within wind direction sector 185–270° (2954 measurements of 10 min mean wind speeds with 97 % data recovery rate) are used for analysis because of flow distortions from the wind turbines and the meteorological mast in the other sectors.

Because of the large data sample, the data are stratified into two wind speed bins 8–12 and 12–16 m s^{-1} (based on V_c), and are sampled in 10° bins of β. When wind speed is between 8 and 12 m s^{-1}, the observed RSE is about 1.5 % for $\beta \sim -90°$ and increases to about 3 % as β approaches −45 and −135° (Fig. 8). The highest RSE occurs at $\beta = -55°$ as the result of the highest wind speed variance in this sector. As at Site A, the predicted RSE obtained using the isotopic turbulence model closely matches the observed RSE when $\beta < -70°$, but underestimates the observed RSE when $\beta > -70°$ possibly due to inhomogeneous flow in this sector from wind turbine wakes, anemometer uncertainty and the low sample size (Fig. 8). Adding the cup anemometer relative error only marginally increases the predicted RSE (Fig. 8).

5.3 Site C

Site C is a wind farm located at 38.1° N in relatively complex terrain. Arc scans were performed over 25 days centered $\theta = 270°$ with $\Delta\theta = 60°$, $\delta\theta = 10°$ and $\phi = 18.05°$

AMTD
8, 10429–10471, 2015

(Fig. 6c). Wind speeds retrieved from range gate 8 are evaluated against a cup anemometer deployed on a boom oriented to 247.5° at 80 m on the meteorological mast southwest of the lidar (Fig. 6c). There is no flow distortion in the wind direction sector 205–290°. However, because of orographic channeling, 95 % of the observations are associated with wind directions between 260 and 290°. Thus, this sector, which contains 2167 measurements of 10 min mean wind speed (93 % data recovery rate), is chosen for the uncertainty analysis.

The observed RSE estimated for 2° bins of β and wind speed between 6 and 14 m s^{-1} indicate a dependence on wind direction which derives largely from the directional variability of the mean and variance of the wind speed (Fig. 9). $\hat{\varepsilon}$ increases from 2 % for $\beta \sim -10°$ to nearly 4 % at $\beta \sim +12°$ in large part due to the decrease in mean wind speed (from 11 to approx. 9 m s^{-1}) and increase in variance (from < 0.6 to nearly 1 m^2 s^{-2}). The observed RSE is consistently higher than the predicted RSE derived from the isotropic turbulence model (by a factor of approximately 1.5) likely because of the cup anemometer uncertainty in complex terrain. After adding the relative error of the cup anemometer to the predicted RSE, the prediction matches closely to the observed RSE. Furthermore, non-homogeneous horizontal wind fields over complex terrain can cause violation of the assumptions made in the theoretical analysis and result in discrepancy between the observed and predicted RSE (Bingöl et al., 2009).

6 Discussion

The isotropic turbulence model is not a true representation of the turbulent wind field in the atmosphere. The three wind components rarely have equal variance and the same turbulence integral length scale. Further, the exponential decay function is only an approximation of the turbulence autocorrelation function. Nevertheless, the analyses presented above indicate that when properly constrained, the isotropic turbulence model reproduces the uncertainty in the wind speed estimated from arc scans with different scanning geometries at different sites, and the predicted relationship between

AMTD
8, 10429–10471, 2015

RSE and turbulence intensity is also consistent with the observed relationship (Fig. 10). The effect of the arc span on the estimated wind speed uncertainty from arc scans as presented based on the theoretical approach can also be verified by observations after they have been normalized to remove the effect of sample number, turbulence intensity and wind speed on the uncertainty to allow comparison across the sites. Thus the relative errors (e_r) are scaled using (Wyngaard, 2010):

$$e_{rN} = \frac{e_r}{S_1 \cdot S_2 \cdot S_3} \tag{21}$$

where

- $S_1 = (M_{10})^{-1/2}$ represents the relationship between the uncertainty and the sample number M_{10} used to derive the mean horizontal wind speed.
- $S_2 = \mathrm{TI}$ accounts for the fact that the uncertainty scales with the turbulence intensity.
- $S_3 = L_u/600\,\mathrm{s} \cdot V_0$ represents the spatial coverage of a measurement over 600 s (10 min) relative to the turbulence integral length scale.

The standard deviations of the errors, when e_{rN} is rescaled back to e_r with $V_0 = 9\,\mathrm{m\,s^{-1}}$, $\mathrm{TI} = 12\,\%$ ($L_u = 209\,\mathrm{m}$ according to Appendix A) and $M_{10} = 40$ using Eq. (21), are 2.3, 2.8 and 6.3 % for Site A, Site C and Site B, respectively. In other words, the uncertainty increases when $\Delta\theta$ decreases from 120° at Site A to 30° at Site B, which is consistent with the predicted relationship between $\Delta\theta$ and RSE given in Fig. 5. This implies this approach presented in Sects. 3 and 4 may be of great use for lidar scan geometry optimization for a given site.

7 Implications for applications in wind energy

If wind speed measurements deriving from arc scans of a lidar are used to predict annual energy production (AEP) at a given site, naturally, the uncertainty in the wind

AMTD
8, 10429–10471, 2015

speeds will propagate into the AEP prediction and contribute to the uncertainty in wind resource assessment. An estimation of that uncertainty can be derived as follows: energy per unit area produced by a wind turbine with wind speed V_i over 10 min is defined as

$$E(V_i) = \frac{1}{2}\rho C_p(V_i)V_i^3 \cdot 600\,\mathrm{s} \tag{22}$$

where ρ is the air density. The power coefficient C_p is a function of wind speed. The AEP is then calculated using the following equation:

$$\mathrm{AEP} = T_y \sum_{j=1}^{J} \sum_{i=1}^{I} E(V_i)P_{ij} \tag{23}$$

where T_y is the total number of 10 min periods in a year and P_{ij} is the probability of the ith wind speed bin in the jth wind direction bin denoted as D_j. Given a wind speed distribution density function $f(V)$ and wind direction distribution density function $g(D)$,

$$P_{ij} = [f(V_i)\Delta V][g(D_j)\Delta D] \tag{24}$$

where ΔV and ΔD are the bin widths for the wind speed and direction, respectively. Given a standard error $\sigma_{\hat{V}_i}$ for V_i, the standard error in AEP (denoted as σ_{AEP}) can then be approximated as

$$\sigma_{\mathrm{AEP}} = \left\{ T_y \sum_{j=1}^{J} \sum_{i=1}^{I} E(V_i)^2 \left[\frac{3}{V_i} + \frac{1}{C_p(V_i)} \frac{\partial C_p(V_i)}{\partial V} \right]^2 (\sigma_{\hat{V}_i})^2 P_{ij} \right\}^{1/2} \tag{25}$$

under the assumption that the wind speed errors are independent of each other (Lyons, 1991).

A scenario analysis of the resulting uncertainty in AEP is undertaken under the following assumption (1) the wind speed follows a Rayleigh distribution with a mean of

AMTD
8, 10429–10471, 2015

$7\,m\,s^{-1}$, (2) the wind direction follows a von Mises distribution with a mean of 90° (see Appendix B for the probability density functions), (3) arc scans centered at $\theta = 90°$ with 6 beams, and $\phi = 15°$, and (4) the hub-height is 80 m. Turbulence intensity and turbulence integral length scale are estimated from the surface roughness using Eqs. (A3) and (A12) in Appendix A, respectively.

The AEP prediction uncertainty calculated using Eqs. (23) and (25) with a C_p curve from a commercial wind turbine is shown in Fig. 11. Because of the large number of samples used for AEP prediction ($T_y = 52\,560$), the AEP RSE defined as σ_{AEP}/AEP is very low (0.05–0.2 %). The uncertainty in AEP increases linearly with TI (and hence z_0) and decreases with increasing arc span. The normalized AEP RSE, which is the ratio of the AEP RSE of arc scans to that of 6-beam conical scans (or $\Delta\theta = 360°$), has the highest value of about 1.4 for $\Delta\theta = 30°$ (Fig. 11c and d). With increasing wind direction variation, both the absolute and normalized AEP RSE of $\Delta\theta = 30°$ remain almost the same, but those associated with $\Delta\theta \geq 60°$ decrease. The AEP RSE for $\Delta\theta = 120°$ is about 5–10 % higher than that of conical scans. Note the uncertainty of conical scans is the minimum value of uncertainty that arc scans can achieve (as a result of $\Delta\theta \rightarrow 360°$).

8 Conclusions

Wind speeds measured by lidars are subject to uncertainties that originate from the prevailing atmospheric conditions, the lidar scanning geometry and the wind velocity retrieval method. The analyses presented herein assume horizontal homogeneity and zero mean vertical velocity, and thus neglect their roles in dictating optimal lidar operation. The effects of the atmospheric turbulence properties and the scanning geometry on the uncertainty in the wind speed estimated from lidar arc scans are investigated with both theoretical predictions and actual observations. The theoretical predictions are based on the frozen turbulence hypothesis and an isotropic turbulence model, and the actual observations include arc scan measurements from different scanning ge-

AMTD
8, 10429–10471, 2015

ometries both onshore and offshore. The predictions and the observations are consistent, and may be summarized as follows:

- The uncertainty can be scaled with the turbulence intensity.
- The lowest uncertainty can be achieved by aligning the line of sight with the wind direction. The highest uncertainty occurs when the wind direction is 45° relative to the line of sight. There is a statistical local minimum of uncertainty when orthogonal scans exist, though the uncertainty associated with the radial velocity increases in the sense that the radial velocity approaches zero but the uncertainty remains unchanged when the relative angle approaches 90°.
- The uncertainty can generally be reduced by increasing the arc span and decreasing the beam number. The reduction is the most significant when the relative angle between the wind direction and the lines of sight is 45°. If the relative angle is close to zero, adjusting the scan geometry will not change the uncertainty significantly. With orthogonal scans, the uncertainty is more sensitive to the beam number than the arc span.
- When the arc scan is used for wind resource assessment, the uncertainty in the annual energy production prediction is very low. The uncertainty decreases with decreasing surface roughness and turbulence intensity and increasing arc span, and the rate of decrease is faster for low wind direction variability than for high wind direction variability.

The uncertainty estimation approach developed in this paper on the basis of the isotropic turbulence model, through has limits and caveats, is able to predict the effect of wind velocity, turbulence intensity and scan geometry on the arc scan uncertainty at the three sites presented herein. Thus, this approach, although it needs to be further validated by more measurements, may have great utility for a priori optimization of lidar scan geometries for a given site.

AMTD
8, 10429–10471, 2015

Appendix A: Atmospheric boundary layer turbulence characteristics

In the neutrally stratified surface layer of the atmospheric boundary layer (ABL), the vertical profile of the horizontal wind speed is given by the logarithmic wind profile (Stull, 1988):

$$V_0(z) = \frac{u_*}{\kappa} \ln\left(\frac{z}{z_0}\right) \tag{A1}$$

where u_* is the surface friction velocity, z_0 is the surface roughness length, $\kappa = 0.4$ is the von Kármán constant and z is the height above the ground. The standard deviation of the horizontal wind speed (σ_u) normalized by the friction velocity is a constant, that is,

$$\frac{\sigma_u}{u_*} = c_n \tag{A2}$$

where the constant $c_n = 2.5$ (Stull, 1988). Hence, according to Eqs. (A1) and (A2), the turbulence intensity, defined as $\mathrm{TI} = \sigma_u / V_0$ can be estimated using the following equation

$$\mathrm{TI} = \frac{c_n \kappa}{\ln(z/z_0)} \tag{A3}$$

The turbulence integral length scale is defined as

$$L_u = \frac{1}{\sigma_u^2} \int_0^{+\infty} c_u(p)\mathrm{d}p \tag{A4}$$

Based on the von Kármán model and the Kolmogorov's 5/3 law, for turbulence with high wave numbers (e.g. turbulence in the inertial subrange), L_u in the atmospheric

AMTD
8, 10429–10471, 2015

surface layer (L_{us}) is defined as

$$L_{us} = c_1 \frac{\sigma_u^3}{\varepsilon_T} \tag{A5}$$

Where $c_1 = 0.7$ (Banakh et al., 1995; Frehlich and Cornman, 2002). The turbulence kinetic energy dissipation rate (ε_T) is related to the dimensionless dissipation rate (ϕ_ε) via the following equation:

$$\varepsilon_T = \frac{\phi_\varepsilon u_*^3}{\kappa z} \tag{A6}$$

For a neutrally stratified atmosphere $\phi_\varepsilon = 1$ (Panofsky and Dutton, 1984). Thus, combining Eqs. (A2), (A5) and (A6) yields a linear relationship between the turbulence integral length scale and the height in the neutrally stratified surface layer:

$$L_{us} = c_1 c_n^3 \kappa z \tag{A7}$$

The actual turbulence integral length scale in the ABL is constrained by the ABL height (z_i) and the following equation can be used to account for the effect of z_i on L_u:

$$L_u(z) = \frac{L_{us}(z)}{1 + c_2 \frac{L_{us}(z)}{z_i}} \tag{A8}$$

where $c_2 = 2.5$ (Blackadar, 1962; Banakh et al., 1995). The height of the neutrally stratified ABL can be determined using the following equation:

$$z_i = c_z \frac{u_*}{f_0} \tag{A9}$$

where the coefficient $c_z = 0.07$–0.3 in the literature (Seibert et al., 2000) and we use $c_z = 0.3$ in this paper. The term f_0 is the Coriolis parameter and defined as

$$f_0 = 2\Omega \sin \phi_L \tag{A10}$$

AMTD
8, 10429–10471, 2015

where ϕ_L is the latitude and $\Omega = 7.292 \times 10^{-5}\,\mathrm{rad\,s^{-1}}$ is the angular speed of the Earth. Combing Eqs. (A2), (A7) and (A8) yields the following formula:

$$L_u = \frac{c_1 c_n^3 \kappa z}{1 + \frac{\kappa c_1 c_2 c_n^4}{c_z} \frac{f_0 z}{\sigma_u}} \tag{A11}$$

Using the values assigned to these empirical coefficients, L_u can be calculated using the following equation:

$$L_u = \frac{4.375 z \sigma_u}{\sigma_u + 91.146 f_0 z} \tag{A12}$$

Appendix B: Wind speed and direction probability distributions

The wind speed distribution can be modeled using the Rayleigh distribution which has the following probability density function (Forbes et al., 2011):

$$f_V(V) = \frac{2V}{A^2} \exp\left[-\left(\frac{V}{A}\right)^2\right] \tag{B1}$$

where A is the scale factor and $A = \sqrt{4/\pi}\overline{V}$ where $\overline{V}$ is the mean wind speed.

The wind direction distribution can be modeled by the von Mises distribution which has the following probability density function (Forbes et al., 2011):

$$f_D(D) = \frac{\exp[b\cos(D - \overline{D})]}{2\pi I_0(b)} \tag{B2}$$

where $D \in [0, 2\pi]$ is the wind direction, $\overline{D}$ is the mean wind direction, b is the concentration parameter, and $I_0(\cdot)$ is the modified Bessel function of the first kind of order zero.

AMTD
8, 10429–10471, 2015

The circular standard devation (σ_D^2) of the wind direction is then defined as

$$\sigma_D^2 = 1 - I_1(b)/I_0(b) \tag{B3}$$

where $I_1(\cdot)$ the modified Bessel function of the first kind of order one.

Acknowledgements. This work was funded by the US National Science Foundation under the award No. 1464383 and the US Department of Energy under the Award No. DE-EE0005379. The insightful comments from the reviewers are acknowledged.

References

Ahn, S. and Fessler, J. A.: Standard Errors of Mean, Variance, and Standard Deviation Estimators, available at: http://ai.eecs.umich.edu/~fessler/papers/files/tr/stderr.pdf (last access: 1 October 2015), University of Michigan, Communication and Signal Processing Lab, Department of EECS, Ann Arbor, Michigan, 2003.

Aitken, M. L., Banta, R. M., Pichugina, Y. L., and Lundquist, J. K.: Quantifying wind turbine wake characteristics from scanning remote sensor data, J. Atmos. Ocean. Tech., 31, 765–787, doi:10.1175/JTECH-D-13-00104.1, 2014.

Banakh, V. A., Smalikho, I. N., Köpp, F., and Werner, C.: Representativeness of wind measurements with a cw Doppler lidar inthe atmospheric boundary layer, Appl. Optics, 34, 2055–2067, doi:10.1364/AO.34.002055, 1995.

Banta, R. M., Pichugina, Y. L., Kelley, N. D., Jonkman, B., and Brewer, W. A.: Doppler lidar measurements of the great plains low-level jet: applications to wind energy, IOP C. Ser. Earth Env., 1, 12–20, 2008.

Banta, R. M., Pichugina, Y. L., Kelley, N. D., Hardesty, R. M., and Brewer, W. A.: Wind energy meteorology: insight into wind properties in the turbine–rotor layer of the atmosphere from high-resolution Doppler lidar, B. Am. Meteorol. Soc., 94, 883–902, doi:10.1175/BAMS-D-11-00057.1, 2013.

Barthelmie, R. J., Crippa, P., Wang, H., Smith, C. M., Krishnamurthy, R., Choukulkar, A., Calhoun, R., Valyou, D., Marzocca, P., Matthiesen, D., Brown, G., and Pryor, S. C.: 3-D wind and turbulence characteristics of the atmospheric boundary layer, B. Am. Meteorol. Soc., 95, 743–756, doi:10.1175/BAMS-D-12-00111.1, 2013.

AMTD
8, 10429–10471, 2015

Bingöl, F., Mann, J., and Foussekis, D.: Conically scanning lidar error in complex terrain, Meteorol. Z., 18, 189–195, 2009.
Blackadar, A. K.: The vertical distribution of wind and turbulent exchange in a neutral atmosphere, J. Geophys. Res., 67, 3095–3102, doi:10.1029/JZ067i008p03095, 1962.
Calhoun, R., Heap, R., Princevac, M., Newsom, R., Fernando, H., and Ligon, D.: Virtual towers using coherent Doppler lidar during the Joint Urban 2003 Dispersion Experiment, J. Appl. Meteorol. Clim., 45, 1116–1126, doi:10.1175/JAM2391.1, 2006.
Choukulkar, A., Calhoun, R., Billings, B., and Doyle, J.: Investigation of a complex nocturnal flow in Owens Valley, California using coherent Doppler lidar, Bound.-Lay. Meteorol., 144, 359–378, 2012.
Courtney, M., Peña, A., Wagner, R., Peeringa, J., Brand, A., Gottschall, J., Rettenmeir, A., and Pierella, F.: D4.06 Data Reports and Databases: Data on Coastal and Offshore Wind Measurements, 42, available at: http://www.fp7-marinet.eu/public/docs/D4.06%20Data%20reports%20and%20databases.pdf (last access: 1 October 2015), MARINET, Cork, Ireland, 2014.
Forbes, C., Evans, M., Hastings, N., and Peacock, B.: Statistical Distributions, John Wiley & Sons, Hoboken, New Jersey, 230 pp., 2011.
Frehlich, R.: Effects of wind turbulence on coherent Doppler lidar performance, J. Atmos. Ocean. Tech., 14, 54–75, 1997.
Frehlich, R.: Estimation of velocity error for Doppler lidar measurements, J. Atmos. Ocean. Tech., 18, 1628–1639, 2001.
Frehlich, R. and Cornman, L.: Estimating spatial velocity statistics with coherent Doppler lidar, J. Atmos. Ocean. Tech., 19, 355–366, doi:10.1175/1520-0426-19.3.355, 2002.
Frehlich, R. and Yadlowsky, M.: Performance of mean-frequency estimators for Doppler radar and lidar, J. Atmos. Ocean. Tech., 11, 1217–1230, 1994.
Frehlich, R., Meillier, Y., Jensen, M. L., Balsley, B., and Sharman, R.: Measurements of boundary layer profiles in an urban environment, J. Appl. Meteorol. Clim., 45, 821–837, doi:10.1175/JAM2368.1, 2006.
Friis Pedersen, T., Dahlberg, J.-Å., and Busche, P.: ACCUWIND-Classification of Five Cup Anemometers According to IEC 61400-12-1, Forskningscenter Risøe, Denmark, Risøe-R, No. 1556(EN), 2006.

AMTD
8, 10429–10471, 2015

Gottschall, J., Courtney, M. S., Wagner, R., Jørgensen, H. E., and Antoniou, I.: Lidar profilers in the context of wind energy – a verification procedure for traceable measurements, Wind Energy, 15, 147–159, doi:10.1002/we.518, 2012.
Henke, M. and Clive, P.: Robust low cost offshore power curve tests with LiDAR, in: EWEA Offshore 2015, 172, Copenhagen, Denmark, 10–12 March 2015.
IEC: IEC 61400-12-1: 2005 Wind turbines – Part 12-1: Power Performance Measurements of Electricity Producing Wind Turbines, Geneva, Switzerland, 90 pp., 2005.
Krishnamurthy, R., Calhoun, R., Billings, B., and Doyle, J.: Wind turbulence estimates in a valley by coherent Doppler lidar, Meteorol. Appl., 18, 361–371, doi:10.1002/met.263, 2011.
Krishnamurthy, R., Choukulkar, A., Calhoun, R., Fine, J., Oliver, A., and Barr, K. S.: Coherent Doppler lidar for wind farm characterization, Wind Energy, 16, 189–206, doi:10.1002/we.539, 2013.
Lindelöw, P., Courtney, M., Parmentier, R., and Cariou, J.: Wind shear proportional errors in the horizontal wind speed sensed by focused, range gated lidars, IOP C. Ser. Earth Env., 1, 012023, doi:10.1088/1755-1315/1/1/012023, 2008.
Lyons, L.: A Practical Guide to Data Analysis for Physical Science Students, Cambridge University Press, Cambridge, UK, 95 pp., 1991.
Monin, A. S. and Yaglom, A. M.: Statistical Hydromechanics, Nauka, Moscow, 1965.
Panofsky, H. A. and Dutton, J. A.: Atmospheric turbulence: models and methods for engineering aplications, John Wiley & Sons, New York, USA, 1984.
Pearson, G. N. and Collier, C. G.: A pulsed coherent CO_2 lidar for boundary-layer meteorology, Q. J. Roy. Meteor. Soc., 125, 2703–2721, doi:10.1002/qj.49712555918, 1999.
Pichugina, Y. L., Banta, R. M., Brewer, W. A., Sandberg, S. P., and Hardesty, R. M.: Doppler lidar-based wind-profile measurement system for offshore wind-energy and other marine boundary layer applications, J. Appl. Meteorol. Clim., 51, 327–349, 2012.
Schwiesow, R., Köpp, P., and Werner, C.: Comparison of CW-lidar-measured wind values obtained by full conical scan, conical sector scan and two-point techniques, J. Atmos. Ocean. Tech., 2, 3–14, 1985.
Seibert, P., Beyrich, F., Gryning, S.-E., Joffre, S., Rasmussen, A., and Tercier, P.: Review and intercomparison of operational methods for the determination of the mixing height, Atmos. Environ., 34, 1001–1027, 2000.

AMTD
8, 10429–10471, 2015

Simley, E., Pao, L. Y., Frehlich, R., Jonkman, B., and Kelley, N.: Analysis of light detection and ranging wind speed measurements for wind turbine control, Wind Energy, 17, 413–433, doi:10.1002/we.1584, 2013.

Stull, R. B.: An Introduction to Boundary Layer Meteorology, Springer Science & Business Media, Dordrecht, the Netherlands, 670 pp., 1988.

Wagner, R., Courtney, M., Gottschall, J., and Lindelöw-Marsden, P.: Accounting for the speed shear in wind turbine power performance measurement, Wind Energy, 14, 993–1004, doi:10.1002/we.509, 2011.

Wang, H., Barthelmie, R. J., Clifton, A., and Pryor, S. C.: Wind measurements from arc scans with Doppler wind lidar, J. Atmos. Ocean. Tech., doi:10.1175/JTECH-D-14-00059.1, 2015.

Wyngaard, J. C.: Turbulence in the Atmosphere, Cambridge University Press, Cambridge, UK, 2010.

AMTD
8, 10429–10471, 2015

Table 1. Galion G4000 Doppler wind lidar specification[1].

Parameter	Value
Wave length	1.56 µm
Pulse energy	30 µJ
Pulse duration[2]	200 ns (30 m)
Range gate size	30 m
Spatial Resolution[3]	60 m
Aperture diameter	75 mm
Pulse repetition frequency	20 kHz
Sampling frequency	100 MHz
Dwell time	1 s
Radial velocity accuracy	0.1 m s^{-1}

[1] This specification is provided by SgurrEnergy.
[2] Full width at half maximum.
[3] Spatial resolution is the sum of the pulse duration and the range gate size (Frehlich, 1997).

AMTD
8, 10429–10471, 2015

Table 2. Uncertainty classification of the cup anemometers used at the three sites.

Site	Cup Anemometer	IEC Class[1]	Class Number
Site A	NRG 40C	A	2.40[2]
Site B	Vector L100	A	1.80[2]
Site C	WindSensor P2546A	B	3.71[3]

[1] Class A is for sites with flat terrains and Class B is for sites with complex terrains (IEC, 2005).
[2] This is based on Friis Pedersen et al. (2006).
[3] This number is given by the cup anemometer manufacturer.

AMTD
8, 10429–10471, 2015

Table C1. Nomenclature.

$\mathbf{A}$	Covariance matrix of the measured radial velocities [$m^2 s^{-2}$]
A	Rayleigh distribution scale factor [$m s^{-1}$]
$\mathbf{C}$	Wind velocity covariance matrix [$m^2 s^{-2}$]
$\hat{\mathbf{C}}$	Covariance matrix of the estimated horizontal wind vector [$m^2 s^{-2}$]
CI_{95}	95 % confidence interval
C_p	Wind turbine power coefficient
D	Wind direction [°]
$\mathbf{D}$	A $N \times 2$ matrix with its ith row given by $[\cos\phi \sin\theta_i \cos\phi \cos\theta_i]$
$\overline{D}$	Annual mean wind direction [°]
E	Wind energy per unit area produced over 10 min [J]
$\mathbf{G}$	A $2 \times N$ matrix defined as $(\mathbf{D}^T\mathbf{D})^{-1}\mathbf{D}^T$
$\mathbf{I}$	Identity matrix
I_k	Bessel function of the first kind of order k
K_r	Covariance between two point radial velocities [$m^2 s^{-2}$]
L_u	Turbulence integral length scale in the atmospheric boundary layer [m]
L_{us}	Turbulence integral length scale in the surface layer [m]
M_{10}	Number of arc scans over a 10 min period
M_θ	Number of azimuth angles per arc scan
N	Number of radial velocities measured over a 10 min period
P_{ij}	Probability density at wind speed bin V_i and direction bin D_j
T_h	Total hours in a year
$\boldsymbol{V}_0$	Mean horizontal wind velocity vector [$m s^{-1}$]
$\hat{\boldsymbol{V}}_0$	Estimated mean horizontal wind velocity vector from arc scans [$m s^{-1}$]
$\overline{V}$	Annual mean wind speed [$m s^{-1}$]
V_0	Horizontal mean wind speed [$m s^{-1}$]
$\hat{V}_0$	Estimated horizontal mean wind speed from arc scans [$m s^{-1}$]
V_c	Horizontal mean wind speed from cup anemometers [$m s^{-1}$]
W	Lidar weighting function
a	Covariance between two measured radial velocities [$m^2 s^{-2}$]
b	Von Mises distribution concentration parameter
c_{lk}	An entry of $\mathbf{C}$ [$m^2 s^{-2}$]
c_u	Spatial covariance of the streamwise wind component [$m^2 s^{-2}$]
$\boldsymbol{d}$	Unit directional vector of the line-of-sight of lidar
e	Radial velocity measurement random error [$m s^{-1}$]
e_r	Relative wind speed error of arc scans
e_{rN}	Normalized relative wind speed error of arc scans
f_0	Coriolis parameter [s^{-1}]
f_D	Wind direction probability density function
f_V	Wind speed probability density function
n	Number of samples
$\boldsymbol{p}$	Separation distance vector between two measured radial velocities [m]
$\boldsymbol{q}$	Separation distance vector between two point radial velocities [m]
q	Separation distance between two point radial velocities [m]
q_1	Separation distance in the streamwise direction [m]
q_2	Separation distance in the transverse direction [m]
q_3	Separation distance in the vertical direction [m]
$\boldsymbol{r}$	Radial velocity position vector [m]
r	Lidar range distance [m]

AMTD
8, 10429–10471, 2015

Table C1. Continued.

$\boldsymbol{s}$	The position vector of a point radial velocity [m]
s	Lidar range distance [m]
t	Number of occurrence of a wind speed from a given wind direction
δt	The time interval between two radial velocity measurement [s]
$\boldsymbol{u}$	Instantaneous wind velocity vector [$\mathrm{m\,s^{-1}}$]
u	Instantaneous west–east wind component [$\mathrm{m\,s^{-1}}$]
$\boldsymbol{u}_0$	Mean wind velocity vector [$\mathrm{m\,s^{-1}}$]
u_0	Mean west–east wind component [$\mathrm{m\,s^{-1}}$]
$\hat{u}_0$	Estimated mean west–east wind component [$\mathrm{m\,s^{-1}}$]
u_*	Surface friction velocity [$\mathrm{m\,s^{-1}}$]
v	Instantaneous south–north wind component [$\mathrm{m\,s^{-1}}$]
v_0	The mean south–north wind component [$\mathrm{m\,s^{-1}}$]
$\hat{v}_0$	Estimated mean south–north wind component [$\mathrm{m\,s^{-1}}$]
$\boldsymbol{v}_\mathrm{R}$	Vector of the measured radial velocities over a 10 min period [$\mathrm{m\,s^{-1}}$]
v_R	Volumetrically averaged lidar radial velocity [$\mathrm{m\,s^{-1}}$]
v_r	Point lidar radial velocity [$\mathrm{m\,s^{-1}}$]
w	Instantaneous vertical wind component [$\mathrm{m\,s^{-1}}$]
w_0	Mean vertical wind component [$\mathrm{m\,s^{-1}}$]
w_R	Lidar signal spectrum width in velocity space [$\mathrm{m\,s^{-1}}$]
z	Height [m]
z_i	Atmospheric boundary layer height [m]
ΔD	Wind direction bin size [°]
ΔR	Spatial extent of a radial velocity measurement [m]
ΔV	Wind speed bin size [$\mathrm{m\,s^{-1}}$]
$\Delta \boldsymbol{p}$	Separation distance vector induced by the mean wind velocity [m]
$\Delta\theta$	Arc scan azimuth span [°]
Ω	Earth rotational speed [$\mathrm{s^{-1}}$]
β	Arc scan relative direction [°]
δ	Radial velocity measurement bias [$\mathrm{m\,s^{-1}}$]
δ_{lk}	the Kronecker delta
δt	Time interval between two radial velocity measurements [s]
$\delta\theta$	Arc scan azimuth angle interval [°]
ε	Relative standard error
$\hat{\varepsilon}$	Observed relative standard error
ε_T	Turbulence kinetic energy dissipation rate [$\mathrm{m^2\,s^{-3}}$]
θ	Lidar azimuth angle [°]
ρ_{uv}	Correlation between $\hat{u}_0$ and $\hat{v}_0$
σ_D	Wind direction standard deviation [°]
σ_ε	Standard deviation of radial velocity measurement random errors [$\mathrm{m\,s^{-1}}$]
σ_u^2	Variance of the streamwise wind component [$\mathrm{m^2\,s^{-2}}$]
$\sigma_{\hat{u}_0}$	Standard deviation of the estimated west–east wind component [$\mathrm{m\,s^{-1}}$]
σ_{v_r}	Standard deviation of radial velocities in the lidar probe volume [$\mathrm{m\,s^{-1}}$]
$\sigma_{\hat{v}_0}$	Standard deviation of the estimated south–north wind component [$\mathrm{m\,s^{-1}}$]
δ_V	Standard deviation of the estimated horizontal wind speed [$\mathrm{m\,s^{-1}}$]
ϕ	Lidar elevation angle [°]
ϕ_L	Latitude [°]
ϕ_ε	Dimensionless dissipation rate

AMTD
8, 10429–10471, 2015

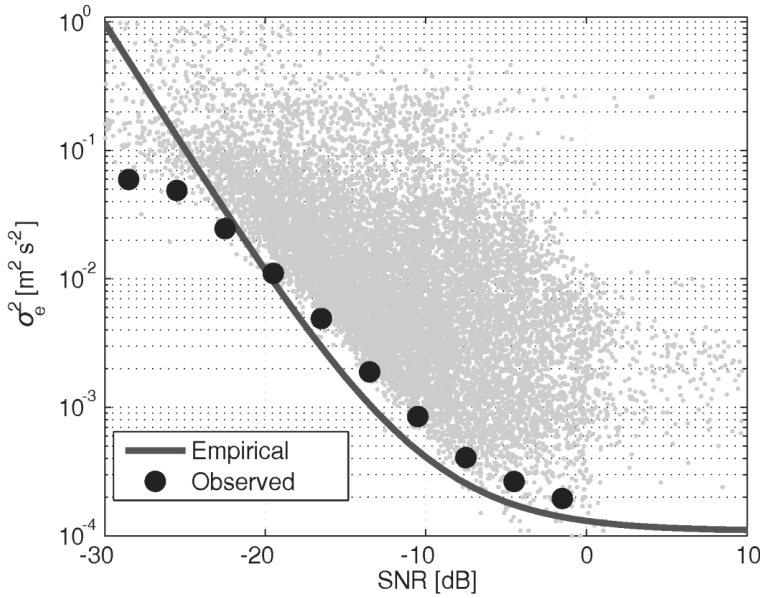

Figure 1. The relationship between the signal-to-noise ratio (SNR) and the radial velocity random error variance (σ_e^2). The gray dots show the observed radial velocity variance approximated by the difference between the variance and the autocovariance at one time lag of the radial velocities collected in an experiment in which the lidar was operated with a staring mode at the US National Renewable Energy Laboratory (Wang et al., 2015), and the observed Cramer–Rao Bound (CRB) (filled dark circles) is approximated by the mean of the lowest 5 % of the gray dots (Frehlich, 2001). The empirical relationship between the SNR and the CRB is denoted by the dark solid line and is based on Eq. (5) in Pearson and Collier (1999).

AMTD
8, 10429–10471, 2015

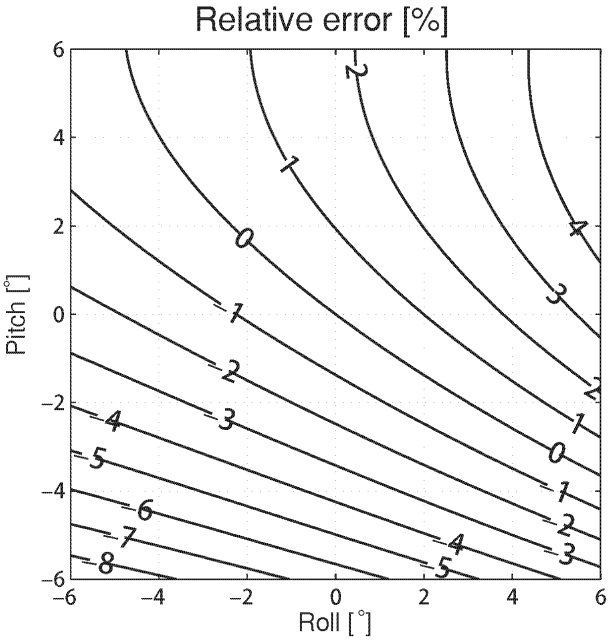

Figure 2. An example of the relative error (%) in the estimated wind speed caused by the pitch and roll of a lidar under the following assumptions: (1) the vertical wind shear is modeled by the power law profile with an exponent of 0.2, (2) the lidar is configured with an elevation angle (ϕ) of 17° and 6 azimuth angles (θ) covering a 30° azimuth span ($\Delta\theta$), (3) the measurement height is 90 m, and (4) wind speed is 7 m s^{-1} and (5) the relative direction (β) is 90°.

AMTD
8, 10429–10471, 2015

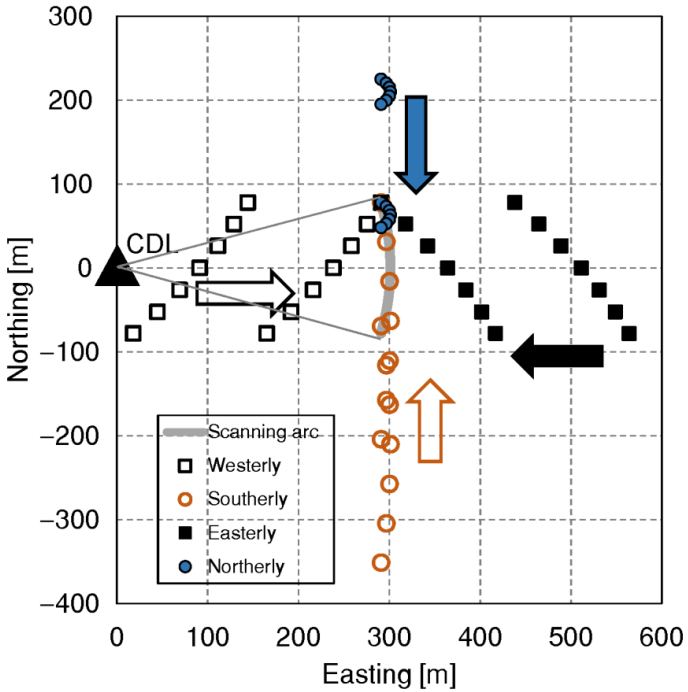

Figure 3. An example of the spatial distribution of air parcels sampled in two consecutive arc scans by a lidar (CDL) at range distance $r = 315$ m for four different wind directions (westerly, easterly, northerly, and easterly) under the following assumptions: (1) frozen turbulence, (2) the lidar is located at the origin (CDL) and scans from $\theta = 75$ to 105° with 5° increments with elevation angle $\phi = 17^{\circ}$, (3) the mean wind speed is 7 m s^{-1} and (4) the sampling interval is 3 s.

AMTD
8, 10429–10471, 2015

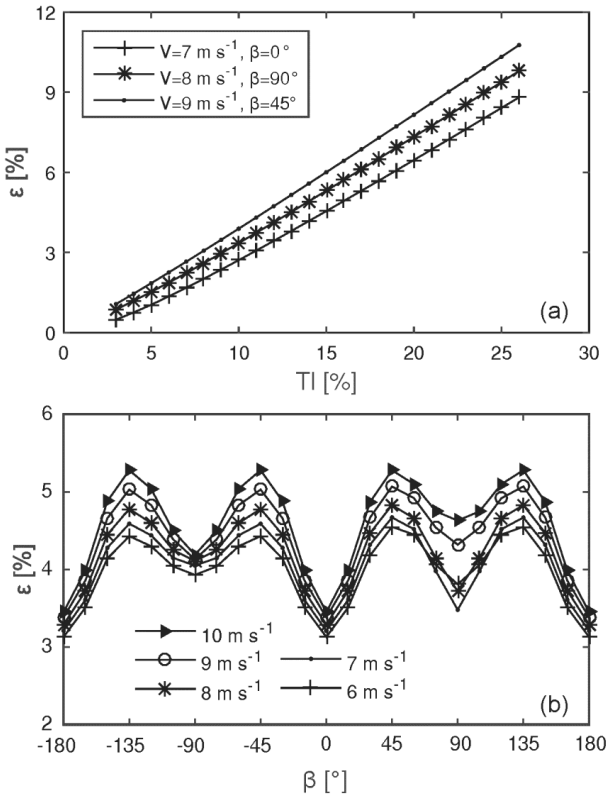

Figure 4. Dependence of the relative standard error (ε) of wind speed estimated from arc scans on **(a)** turbulence intensity (TI) and **(b)** wind speed (V_0) and direction (expressed as the relative direction (β)) based on the isotropic turbulence model given in Eq. (13) for the following scan geometry: $\phi = 16.7^\circ$, $\Delta\theta = 30^\circ$, $\delta\theta = 6^\circ$ and $r = 315\,\mathrm{m}$. The turbulence integral length scale (L_u) is derived using Eq. (A12) with the Coriolis parameter $f_0 = 0.0001\,\mathrm{m\,s^{-1}}$.

AMTD
8, 10429–10471, 2015

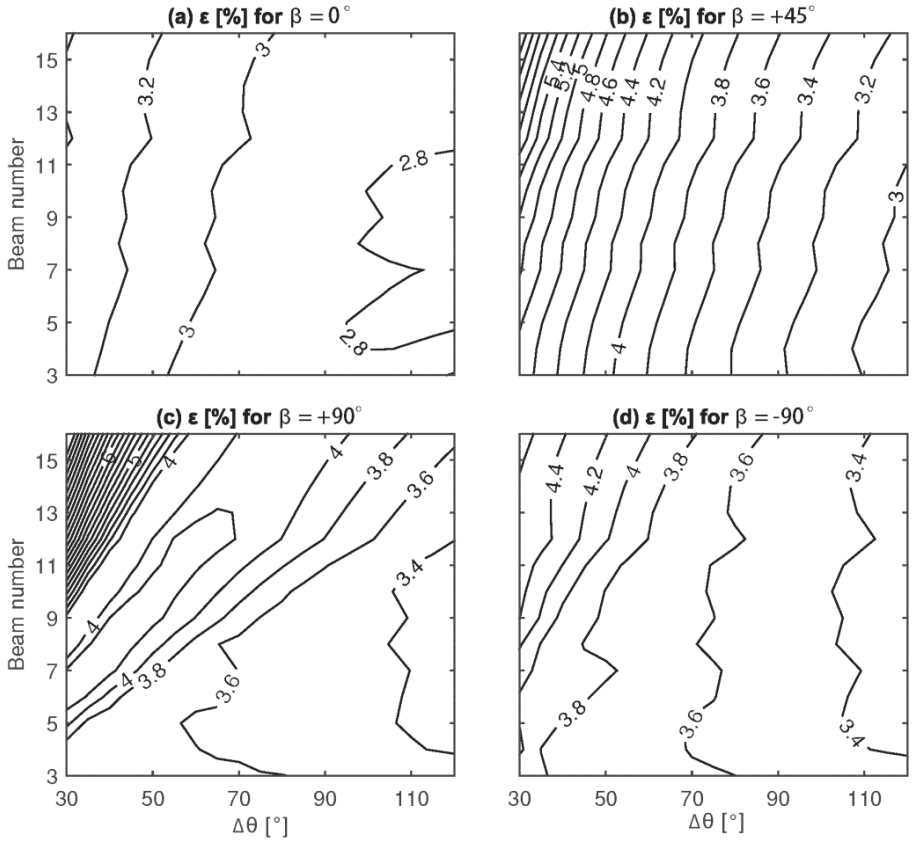

Figure 5. Dependence of the relative standard error (ε) of wind speed (V_0) on the arc span ($\Delta\theta$) and the beam number per arc scan for relative directions **(a)** $\beta = 0^\circ$, **(b)** $\beta = +45^\circ$, **(c)** $\beta = +90^\circ$, and **(d)** $\beta = -90^\circ$ with $\phi = 16.7^\circ$ and $r = 315$ m. The results are calculated for $V_0 = 7\,\mathrm{m\,s^{-1}}$ and TI = 12 % over a 10 min period. The turbulence integral length scale (L_u) is derived using Eq. (A12) with the Coriolis parameter $f_0 = 0.0001\,\mathrm{m\,s^{-1}}$. The contour interval is 0.2 %.

AMTD
8, 10429–10471, 2015

Lidar arc scan uncertainty reduction through scanning geometry optimization

H. Wang et al.

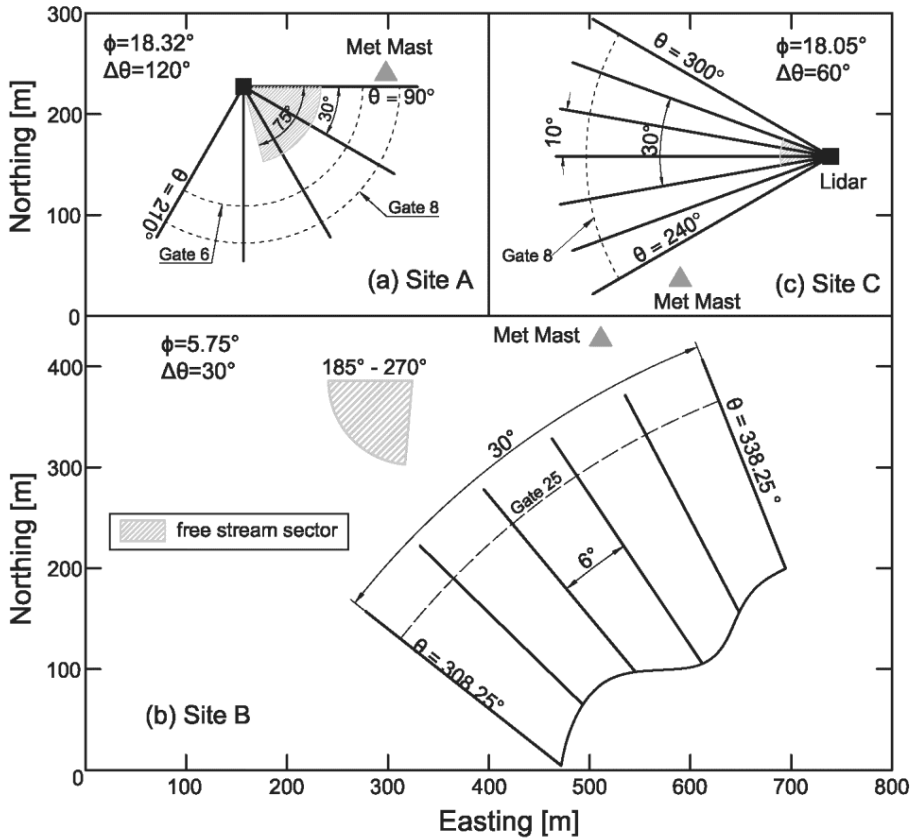

Figure 6. Plan views of the scanning geometries used at **(a)** Site A, **(b)** Site B and **(c)** Site C. CDL indicates the location of the lidar, and the hatched areas indicate the wind direction sectors without flow distortions. Locations of meteorological masts are denoted by the solid gray circles. The elevation angle (ϕ) and the arc span ($\Delta\theta$) used at each of the sites are also given.

AMTD
8, 10429–10471, 2015

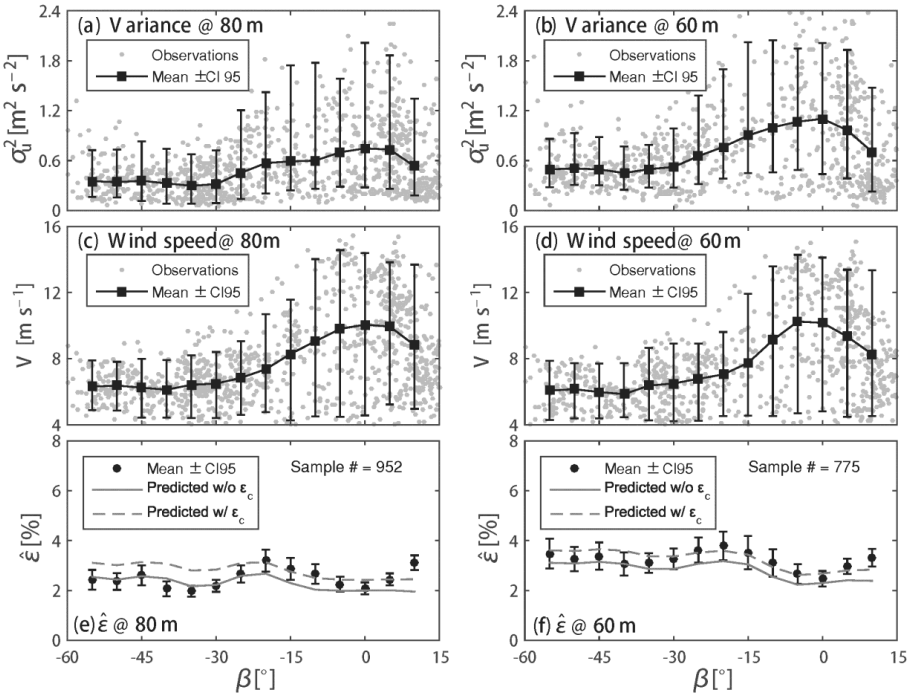

Figure 7. The mean and the 95 % confidence interval (CI_{95}) of the observed relative standard errors ($\hat{\varepsilon}$) at Site A and their variation with the relative direction (β) at 80 m height in (**a**, **c** and **e**) and 60 m height in (**b**, **d** and **f**). The predicted relative standard error from the isotropic turbulence model is denoted by the solid gray lines for prediction without the relative error of cup anemometer (ε_c) and the dashed lines with ε_c in (**e** and **f**). The input for the model predictions include the mean wind speeds (V_0) shown in (**c** and **d**) and the mean wind speed variance (σ_u^2) shown in (**a** and **b**) for 80 m height and 60 m height, respectively. The turbulence integral length scale (L_u) is derived from V_0 and σ_u according to Eq. (A12).

AMTD
8, 10429–10471, 2015

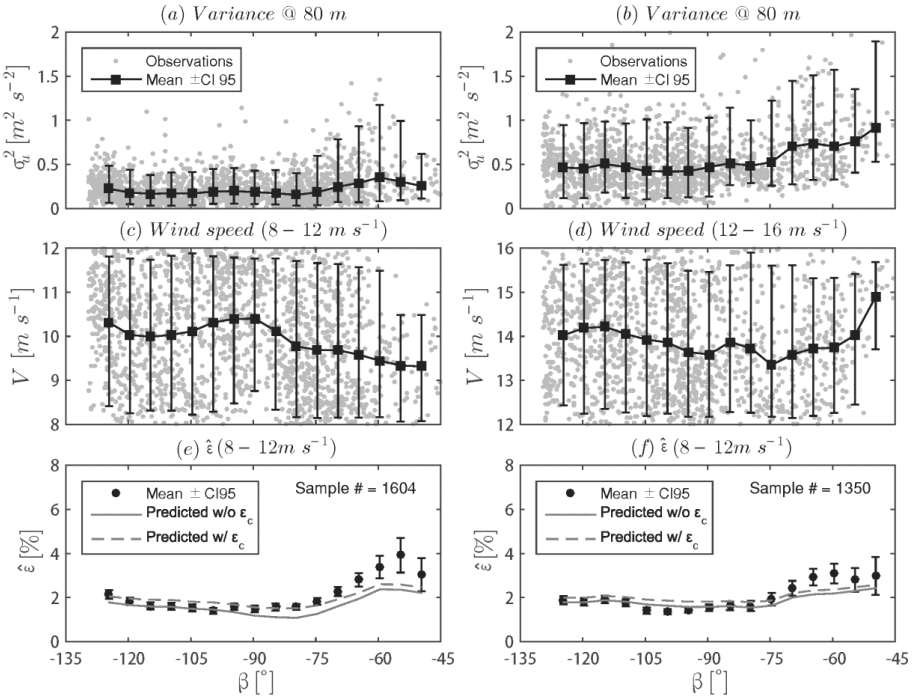

Figure 8. The mean and the 95 % confidence interval (CI_{95}) of the observed relative standard errors ($\hat{\varepsilon}$) at 90 m height at Site B and their variation with the relative direction (β) for the wind speed bin 8–12 m s^{-1} in (**a**, **c** and **e**) and the wind speed bin 12–16 m s^{-1} in (**b**, **d** and **f**). The predicted relative standard error from the isotropic turbulence model is denoted by the solid gray lines for prediction without the relative error of cup anemometer (ε_c) and the dashed lines with ε_c in (**e** and **f**). The input for prediction includes the mean wind speeds (V_0) shown in (**c** and **d**) and the mean wind speed variance (σ_u^2) shown in (**a** and **b**) for wind speed bin 8–12 and 12–16 m s^{-1}, respectively. The turbulence integral length scale (L_u) is derived from V_0 and σ_u according to Eq. (A12).

AMTD
8, 10429–10471, 2015

Lidar arc scan uncertainty reduction through scanning geometry optimization

H. Wang et al.

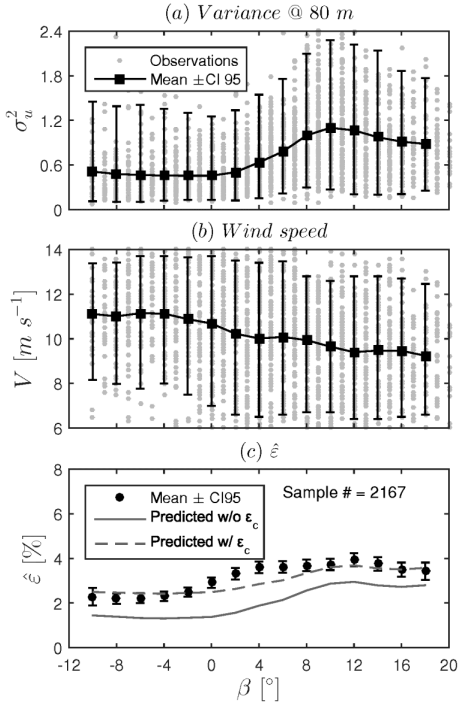

Figure 9. The mean and the 95 % confidence interval (CI_{95}) of the observed relative standard errors ($\hat{\varepsilon}$) at Site C and their variation with the relative direction (β) at 80 m height. The predicted relative standard error from the isotropic turbulence model is denoted by the solid gray line for prediction without the relative error of cup anemometer (ε_c) and the dashed line with ε_c in **(c)**. The input for prediction includes the mean wind speeds (V_0) shown in **(b)** and the mean wind speed variance (σ_u^2) shown in **(a)**. The turbulence integral length scale (L_u) is derived from V_0 and σ_u according to Eq. (A12).

AMTD
8, 10429–10471, 2015

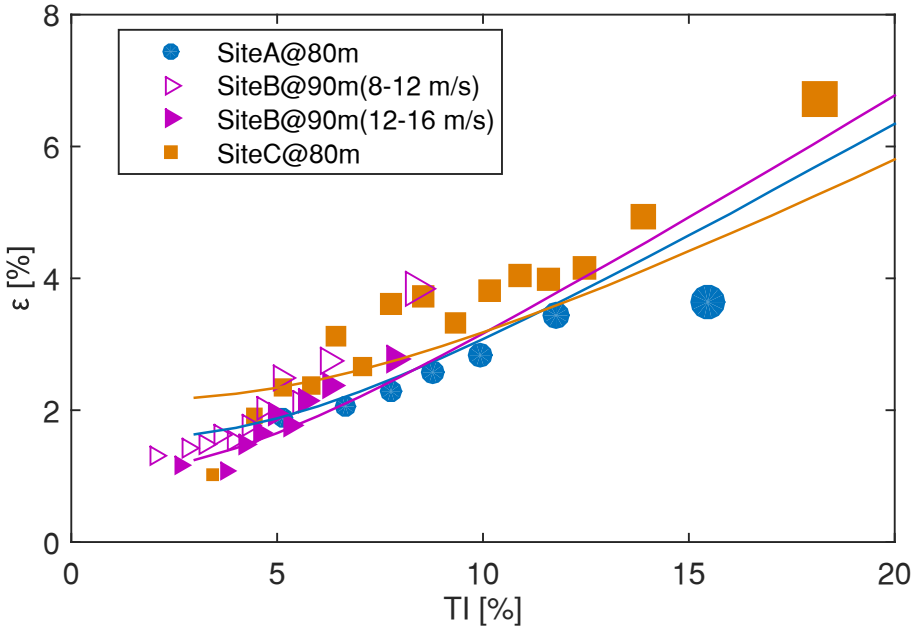

Figure 10. The observed relationship between the relative standard error (ε) and the turbulence intensity (TI) at the three sites. The 95 % confidence interval for each observed ε is denoted by the marker size. The solid lines with matching colors are the predicted relationships at the sites. Prediction at Site A uses wind speed 8 m s^{-1} and wind direction 150°, at Site B wind speed 10 m s^{-1} and wind direction 323°, and at Site C wind speed 10 m s^{-1} and wind direction 270°. The cup anemometer uncertainty has been added to the predicted relative standard error according to Eq. (20) and Table 2.

AMTD
8, 10429–10471, 2015

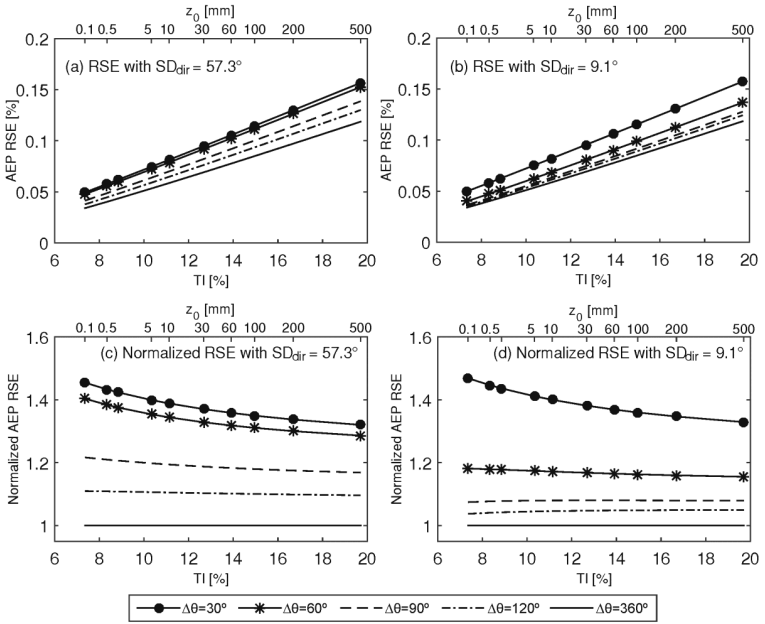

Figure 11. The relative standard error (RSE) in the annual energy production (AEP) predicted as a function of the turbulence intensity (TI) and the surface roughness length (z_0), assuming that the wind speed follows a Rayleigh distribution with a mean of 7 m s^{-1}, and the wind direction follows the von Mises distributions with a mean of 90° and standard deviations (SD_{dir}) of 57.3° in **(a)** and 9.1° in **(b)**. Four arc spans and a full azimuth conical scan (see the legend) are used for AEP prediction with six beams, ϕ = 15° and r = 315 m. The normalized APE RSE, which is the ratio of predicted AEP RSE from arc scans to that from the conical scan, is shown in **(c)** for SD_{dir} = 57.3° and in **(d)** for SD_{dir} = 9.1°. The turbulence intensity and the surface roughness length are related through Eq. (A3).

AMTD
8, 10429–10471, 2015